Synthesis of caged iodine-modified ZnO nanomaterials and study on their visible light photocatalytic antibacterial properties

Yubo Jin, Jintao Long, Xi Ma, Tanghua Zhou, Zizhong Zhang, Huaxiang Lin*, Jinlin Long, Xuxu Wang

College of chemistry of Fuzhou University, State Key Laboratory of Photocatalysis on Energy and Environment, Fuzhou University, Fuzhou, 350116, China

ABSTRACT

The grain size and surface oxygen vacancy concentration of ZnO have great influence on its photocatalytic performance. In this work, caged Iodine-modified ZnO (I-ZnO-n) catalyst with nano-structure and surface oxygen vacancy were successfully prepared by reflux method. The crystal structure, surface properties and optical properties were characterized by XRD, SEM, TEM, RAMAN, ESR and EPR. And the photocatalytic antibacterial activity under visible light has been tested. The results show that the nano-structure I-ZnO-n's band gap is narrow than ZnO because of the existence of oxygen vacancy. And I-ZnO-n exhibits better antibacterial property than micron-structured Iodine-modified ZnO. The ESR and electrochemical experiments confirm that the I-ZnO-n has much more surface oxygen vacancy and higher separation efficiency of photogenic carriers than micron-structured Iodine-modified ZnO, which results its superior photocatalytic performance.

1. Introduction

With the development of science and technology and the gradual improvement of people's living standards, people are fully aware of the importance of the health and demand higher level on living environment. But the threat of diseases caused by bacteria, viruses and other pathogens has never been eliminated. For example, "SARS" in 2003 [1], MERS-Co V in 2015 [2,3] and H_7N_9 [4] and $H_{10}N_8$ [5] viruses in recent years. According to the *Guidelines for Clinical Use of Antibacterials,* the infectious diseases caused by bacteria, viruses and other pathogenic microorganisms spread throughout clinical departments, in which the bacterial infections are one of the most common phenomena. In addition, the breeding of microorganisms will also cause the corruption and deterioration of materials such as food [6], cosmetics [7] and cultural relics [8], and bring significant economic losses and infliction of body to relevant industries and individuals.

Traditional disinfection methods, such as chlorination [9], ozone oxidation [10], UV sterilization [11], high temperature sterilization [12] and so on, can effectively kill most harmful microorganisms. However, chlorination and ozone oxidation produce varieties of harmful carcinogenic by-products, and the use of ultraviolet sterilization and high temperature sterilization has certain limitations. Thus, it is urgent to find safe and efficient antibacterial technique.

Photocatalytic technology is a kind of multi-functional technology with high efficiency of antibacterial activity, which can effectively kill harmful microorganisms in various media [10,13–16]. As a safe material approved by the Food and Drug Administration (21cfr182.8991), ZnO has attracted more and more attention because of its good sterilization and antiviral activity [17]. At present, many literatures about the photocatalytic property of ZnO have been reported [18–23]. There are three main crystal structures of ZnO: wurtzite, zinc-blende and rock-salt. Among them, hexagonal wurtzite-structured ZnO is the most stable under normal pressure and is suitable to be used as a photocatalyst. As a wide band gap semiconductor material, wurtzite-structured ZnO has band gap about 3.37 eV and exhibits excellent photocatalytic activity under UV light illumination [24]. In addition, it has many advantages such as stable chemical properties, safety and non-toxic, bio-adaptability [25]. So, ZnO is potential applied in photocatalytic hydrogen evolution [26], photocatalytic degradation of organic compounds such as dyes [27], photoreduction treatment of heavy metal ions in wastewater [28], photocatalytic antibacterial [29], pollution prevention and fog self-cleaning [30], etc.

However, some disadvantages of ZnO limit its widely application up to now. First, ZnO can only be excited by ultraviolet light that makes it only be applied under UV light illumination. In addition, the photo-generate electron-hole pairs of ZnO are extremely easy to recombine, which greatly reduce the photocatalytic efficiency of ZnO. To improve the photocatalytic efficiency of ZnO, some researchers have proposed

---

* Corresponding author.
  E-mail address: lhx@fzu.edu.cn (H. Lin).

some strategies. Nagarajan Padmavathy suggested that ZnO with smaller particle size has better antibacterial activity [31]. Other researcher reported that nanometer photocatalysts shows higher separation efficiency of photogenic carrier because of its large specific surface area and much more surface active sites [32]. In our previous work, it was found that Iodine-modified ZnO not only exhibits visible light activity, but also has more oxygen vacancies on its surface that is benefit to the separation of photogenic electron-hole pairs [33]. According to the above reports, both particle size and surface oxygen vacancy concentration have significant effect on the photocatalytic activity of ZnO. In order to optimize the antibacterial efficiency of ZnO, Iodide-modified ZnO with nanostructure and oxygen vacancies were synthesized and its structure and visible photocatalytic antibacterial activity were tested.

2. Experiment

2.1. Materials synthesis

Iodine-modified ZnO nanomaterials were synthesized by reflux method. The specific synthesis steps are as follows: 2 mmol HIO_3 and 20 mmol $Zn(NO_3)_2 \cdot 6H_2O$ were mixed in a round-bottom flask. And then 160 mL ethylene glycol (EG) were added to the round-bottom flask and heated to 140 ℃ for 4 h under the oil bath. The continuous magnetic stirring needed during the reaction. After naturally cooling to the room temperature, the product were centrifuged several times with deionized water and ethanol and dried at 60 ℃. The obtained precursor of Iodine-modified ZnO was denoted as pre-I-ZnO-n. The precursor were heated at 500 ℃ for 2 h. The resulting samples were cooled to room temperature and ground to powder. The sample was marked as I-ZnO-n.

In order to compare the property of I-ZnO-n, micron-structured Iodine-modified ZnO (I-ZnO-m) and ZnO were prepared according to our previous work [33]. The specific preparation process is described in the supporting information.

2.2. Materials characterization

The crystalline structures of the as-prepared samples were determined by powder X-ray diffraction(XRD) on a Bruker D8 X-ray diffractometer with Cu Kα radiation(k =0.15418 nm) operating at 40 kV and 40 mA. The scanning step length and scanning rate are respectively set as 0.0198° and 0.05 s/ step. The average particle size of nanomaterials with grain size less than 100 nm was obtained according to the Scherrer formula:

$$D_{\langle hkl \rangle} = K\lambda / (\beta cos\theta) \qquad (2\text{-}1)$$

$D_{\langle hkl \rangle}$: The crystal grain size of (*hkl*); K: The shape factor of the crystal; λ: The wavelength of the x-ray (nm); β: Full width at half maximum; θ: Diffraction angle

The morphologies of samples were observed by a Phenom G2 Pro scanning electron microscope (SEM). Ultraviolet-visible (UV–vis) diffuse reflectance spectra (DRS) of the samples were obtained by using an ultraviolet-visible spectrophotometer (Cary 500), with $BaSO_4$ power as reflectance standard sample. Raman spectra of samples were recorded at room temperature on a Renishaw Invia Raman microscope (Invia Reflex).The microstructure and crystal structure of the samples were observed by Philips tecnai20 FEG transmission electron microscope (TEM). First, a small number of samples were added to ethanol, and the ultrasonic dispersion was carried out. Then, the ultrasonic supernatant was added to the copper network and tested after drying. The Micromeritics 3020M was used to perform Brunauer-Emmett-Teller (BET) analysis. All the samples should be degassed at 250 ℃ for 3 h under vacuum at first. Ultraviolet photoelectron spectroscopy (UPS) studies were carried out by an ESCALAB 250 photoelectron spectroscope (Thermo Fisher Scientific) system which use He I Ultraviolet source(21.22 eV), and the reference use carbonaceous C 1s line (284.6

eV) to calibrate the binding energies (BE). The oxygen vacancy and other defects of solid samples were measured by Bruker A300 electron paramagnetic resonance instrument (EPR). The instrument parameters are set as: Magnetic Field=3400G、Modulation Frequency=100.00 KHz、Microwave Frequency=9.84 GHz、Power=2.0 Mw. Then convert the magnetic field units into g according to the formula:

$$g = h\nu / (\beta B) \qquad (2\text{-}2)$$

Planck's constant = 6.626196×10^{-27} erg.sec ; Bohr facto = 9.2741×10^{-21} erg.Gauss-1

The electron spin resonance (ESR) spectra which capture the •OH produced by the light time catalyst with DMPO were collected on a Bruker model A300 Paramagnetic spectrometer.

2.3. Photoeletrochemical measurements

Photoelectrochemical measurements were carried out through a conventional three-electrode system: Pt plate as the counter electrode, Ag/Agcl electrode as the reference electrode and fluorine-doped tin oxide (FTO) glass as working electrode. A turbid liquid was prepared by dispersing 5 mg of the sample in 0.5 mL of *N,N*-Dimethylformamide (DMF),and then spread it onto FTO glass with an area of 0.5 × 0.5 cm. The FTO glass was insulated with nail polish except where the sample is covered. The exposed area of the working electrode was 0.283 cm^{-1}.The electrolyte in the system used Na_2SO_4 (0.2 M) solution with pH of 6.8. Periodic photocurrent response was measured by illuminating the working electrode with a 300 W Xe arc lamp (λ ≥ 420) (PLS-SXE 300, Beijing Perfect light Co., Ltd.). Mott-Schottky experiments were also measured with this system and the perturbation signal was 10 mV with the frequencies at 0.5, 1.0 and 1.5 KHz, respectively.

2.4. Bacterial cultures and assessment of photocatalytic antibacterial activity

In this section, we choose *E.coli* as a model bacterium to assess the antibacterial activity of the samples. All the containers and solutions used in the experiment were sterilized at 121 ℃ for 30 min in an autoclave. In the experiment, 4 mL bacteria solution (10^8 cfu/ mL) was added to 36 mL PBS solution and *E. coli* solution with an initial concentration of 10^7 cfu/ mL was obtained. 40 mg photocatalyst was added to the solution. After one hour later, 0.5 mL was withdrew and spread on the plates filled with 15 mL fresh nutrient. After nutrient solidification, put plate in the incubator (37 ℃ ± 0.5 ℃) for cultivating 36 h to 48 h. The initial concentration of bacteria liquid is obtained by plate colony counting method. The reaction lasts 4 h. The experiment uses a 300 W Xe arc lamp as light source, and the 420 nm filter was used to filter out the light with a wavelength of less than 420 nm. The current is 12 A and the light intensity above the solution is about 110 mW/ cm^2. A fan was used to prevent the temperature from rising during the experiment.

3. Results and discussion

3.1. X-ray diffraction

Fig. 1 shows the X-ray diffraction (XRD) patterns of I-ZnO-n and I-ZnO-m with the 2 Theta in the range of 20°and 80°. All the peaks of I-ZnO-n and I-ZnO-m can be well matched with the diffraction peaks of hexagonal wurtzite-structured ZnO according to the standard ZnO card (PDF# 36-1451). It indicates that hexagonal wurtzite-structured I-ZnO-n was successfully prepared. Fig. 1b shows the partial enlarged view of X-ray diffraction (XRD) patterns of I-ZnO-n and I-ZnO-m in the range of 30°and 40°. When compared with I-ZnO-m, the peak intensity of I-ZnO-n at 30°to 40°is much weaker and the half peak width is much more broaden. This may be attributable to smaller grain size of I-ZnO-n.
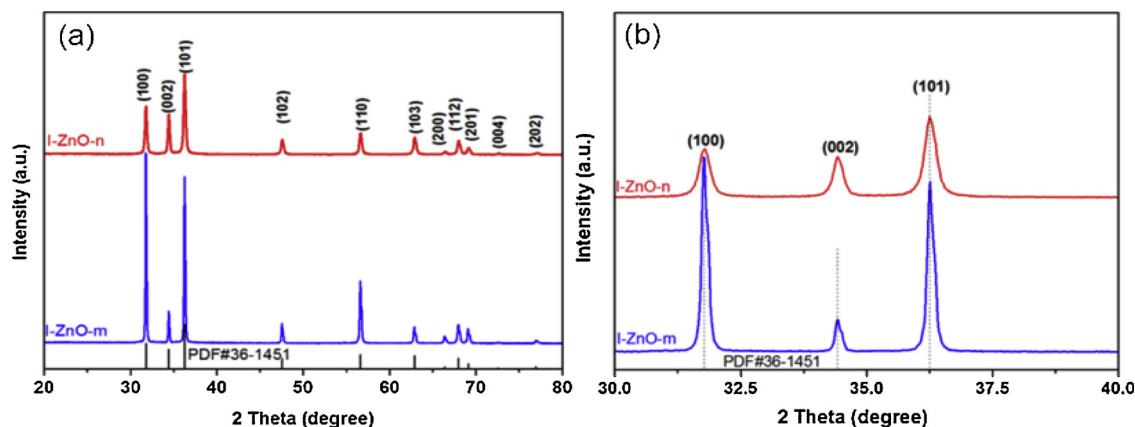
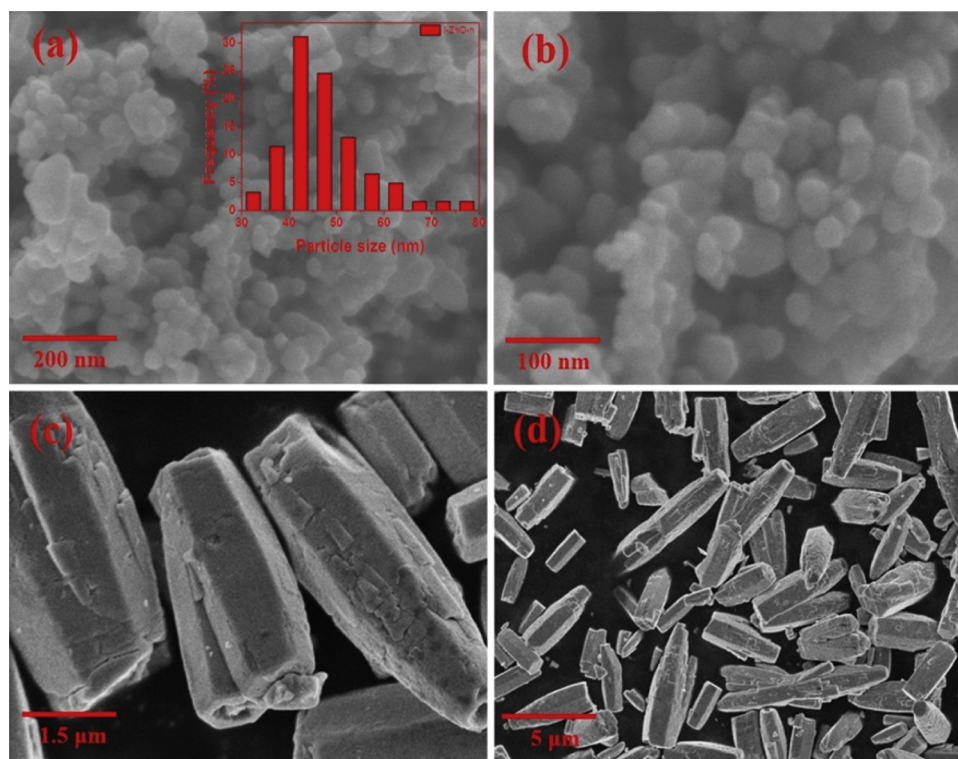**Fig. 1.** X-ray diffraction patterns of samples.

Fig. 2. SEM images of (a)(b) I-ZnO-n, (c)(d)I-ZnO-m.

According to the relevant dimensions of crystal planes of (101) and Scherrer formula, the grain size of I-ZnO-n is calculated about 30.3 nm, which is much smaller than the size of I-ZnO-m. This difference is obvious in SEM analysis. As can be seen from Fig. 2, the particle size distribution of I-ZnO-n is mainly between 30 nm and 50 nm, while the size of I-ZnO-m exhibits rod-structures with the length of them around 5 μm.

3.2. Scanning electron microscope (SEM) and Transmission electron microscope (TEM)

Fig. 2 shows the SEM images of I-ZnO-n and I-ZnO-m. It shows that I-ZnO-n exhibits granular nanostructure and the particle size distribution mainly between 30 nm and 50 nm (Fig. 2a and b). Fig. 2c and d shows that the I-ZnO-m has rod-structure with the lengths about 5 μm. Compared with the surface morphology of ZnO (Fig.S1), the surface of I-ZnO-m is rougher and imperfect, indicating that the addition of Iodine in the preparation process had certain impact on the morphology and structure of ZnO crystals.

Fig. 3 shows the transmission electron microscopy (TEM) images and high resolution transmission electron microscopy (HRTEM) images of I-ZnO-n and I-ZnO-m. I-ZnO-n exhibits very thin sheet and cage structure, while I-ZnO-m shows much more thick sheet and is more fine and close in texture than I-ZnO-n. The cage structure of I-ZnO-n may be resulted from the EG during the prepared process. The •OH in EG can be adsorbed on the positive polar surface of ZnO crystal by Coulomb force, which restricts the growth of ZnO crystal along direction of [001]. Thus the as-prepared sample firstly form nanosheet structure [34]. Then, due to the effect of surface stress of sample, the nanosheet ZnO materials are assembled into cage structure gradually [35,36]. The HRTEM maps (Fig. 3b and d) show that inter-planar spacing of I-ZnO-n and I-ZnO-m is 0.265 nm that is little larger than that of ZnO (0.260 nm) (PDF# 36-1451), suggesting that Iodine species may affect crystal surface structure of ZnO. Figure S2 displays the nitrogen adsorption-desorption isotherms of I-ZnO-n and I-ZnO-m. The BET surface areas, which determined by a multipoint BET method using the adsorption data in the
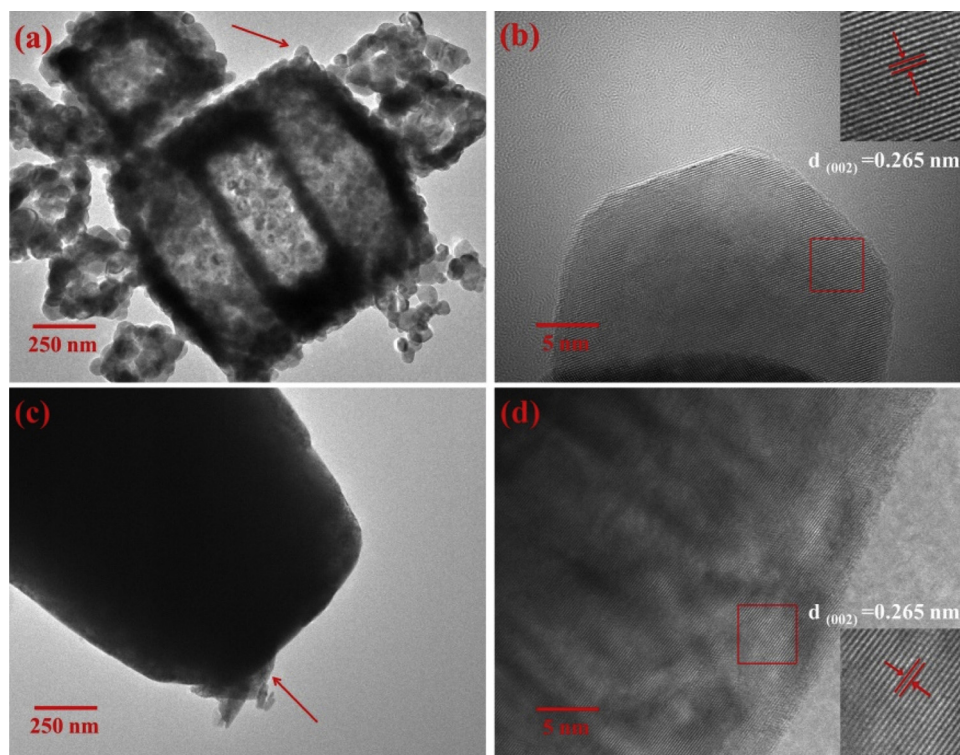
Fig. 3. TEM images of (a)(b)I-ZnO-n, (c)(d)I-ZnO-m.

relative pressure P/P_0 range of 0.05-0.30, are 2.37 $m^2/$ g (I-ZnO-m) and 7.21 $m^2/$ g (I-ZnO-n). This means that I-ZnO-n have a larger specific surface area and provide more active sites for catalytic reactions [36].

3.3. Oxygen vacancies of I-ZnO-n and I-ZnO-m

Fig. 4 shows the Raman spectra of ZnO, I-ZnO-n and I-ZnO-m. The characteristic peaks at 332 cm^{-1}、379 cm^{-1} and 437 cm^{-1} correspond to the multi-phonon scattering process E2 (high)-E2 (low), A1 (TO) and non-polar optical phonons E2 (high) mode of ZnO, respectively [37]. Comparing to ZnO, I-ZnO-n and I-ZnO-m show some differences in the follow features: (i) The characteristic peaks (332 cm^{-1}、379 cm^{-1} and 437 cm^{-1}) that ascribed to ZnO shift to lower wavenumber and the peak width becomes wider. (ii) The peak intensities at 332 cm^{-1}、379 cm^{-1} and 437 cm^{-1} show a greatly decrease, especially the peak at 379 cm^{-1}, almost disappeared. This can be associated with the decrease of the sample's crystalline and grain size or the change of structure. The

disappearance of the 379 cm^{-1} peak is ascribed to that the sample is rich with oxygen vacancies [38]. (iii) The new peaks appeared at the lower wavenumber around 200 cm^{-1} are attributed to Iodine species [39,40]. The peak of Iodine species at 165 cm^{-1} is assigned to I_n-$(n \geq 5)$ (ν_1) and the peak at 216 cm^{-1} is ascribed to I_3- (ν_1), respectively. This phenomenon suggests that the Iodine modification has affected the structure of ZnO to some extent, and Iodine modification on ZnO enhance the concentration of oxygen vacancies.

The oxygen vacancies on I-ZnO-n and I-ZnO-m are confirmed by solid EPR spectrum. As shown in Fig. 5, the paramagnetic signal near $g = 2.002$ is generally ascribed to oxygen vacancy of the bound single electron (VO^+) that resulted from surface defects of samples [41]. As can be seen in the spectra, the signal intensity of I-ZnO-n is much stronger than that of I-ZnO-m, which indicates the I-ZnO-n has much more oxygen vacancies on its surface. This difference may result in different concentration of free radicals produced by the two catalysts in the photocatalytic process.
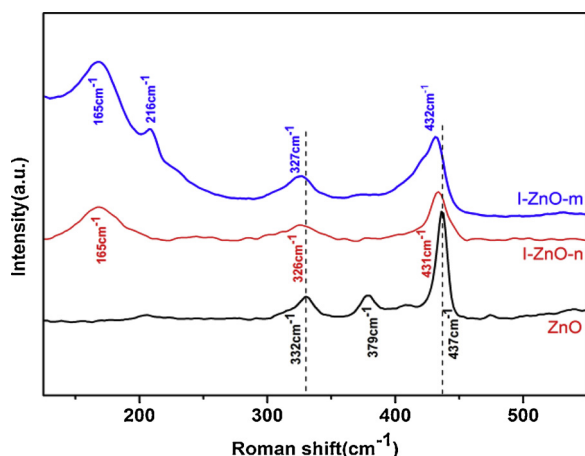

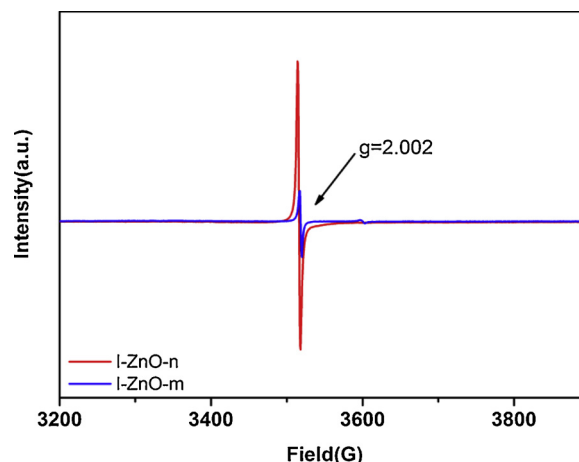**Fig. 4.** Raman spectra of I-ZnO-m, I-ZnO-n and ZnO.
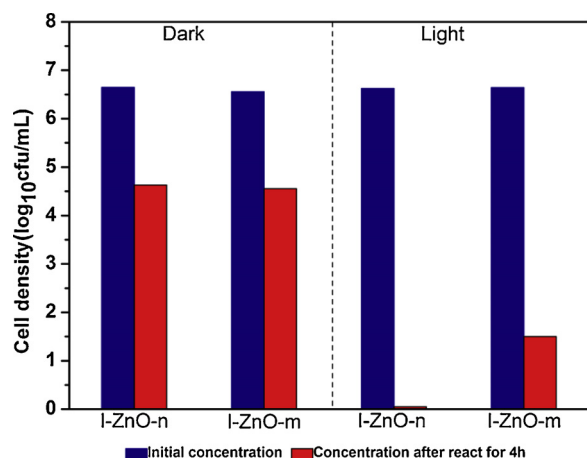

Fig. 5. EPR spectra for I-ZnO-n and I-ZnO-m.

Fig. 6. Photocatalytic inactivation of *E. coli* (3.2×10^6 cfu/ mL) with I-ZnO-n and I-ZnO-m under visible light irradiation.

3.4. Photocatalytic sterilization performance

The photocatalytic disinfection activity of samples was shown in Fig. 6. Both I-ZnO-n and I-ZnO-m show very weak antibacterial activity in dark and the bacterial concentration declined less than 10^2 cfu after reaction for 4 h. But under light conditions, the two samples show different antimicrobial activity. In I-ZnO-n system, the bacteria concentration drops to 10^0 cfu and all bacteria are inactivated in the presence of visible light irradiation. However, I-ZnO-m can only inactivate about 10^5 cfu bacteria after 4 h irradiation. The antibacterial activity of I-ZnO-n is 10 times of that of I-ZnO-m, indicating that I-ZnO-n has better antibacterial performance than I-ZnO-m.

During the photocatalytic process, the reactive oxidative species (such as $\cdot O^{2-}$ and $\cdot OH$) and the photo-generated h^+ and e- are the reactive species, and their concentration is crucial to the photocatalytic efficiency. The efficient separation of h^+ and e^+ is the most significant factor [42]. The photo-generated h^+ and e^- not only directly attacks the bacteria but also generate other reactive oxidative species, such as $\cdot O^{2-}$, $\cdot OH$ and H_2O_2 that can activate the bacteria. The separation and migration of photogenerated carriers are usually assessed by the photocurrent test. The higher the photocurrent intensity, the higher the carrier separation efficiency [43]. As can be seen from Fig. 7, when the light was turned on, the photocurrent density of both samples increased sharply and the photocurrent density of I-ZnO-n is much stronger than I-ZnO-m. This indicates that the charge separation efficiency of I-ZnO-n is better than that of I-ZnO-m. In addition, when the light was turned
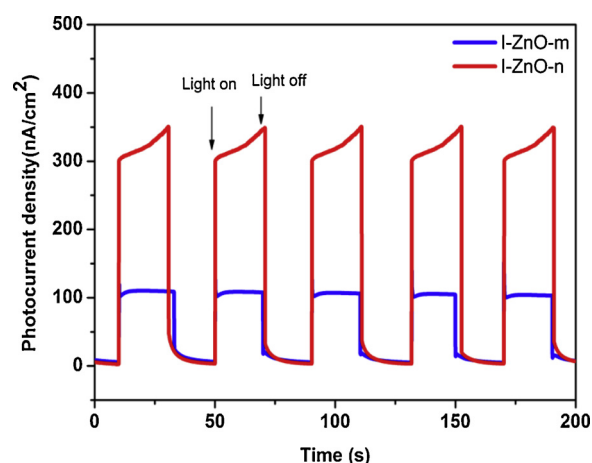

Fig. 7. Photocurrent density of I-ZnO-m and I-ZnO-n under visible light irradiation ($\lambda \geq 420$ nm).

off, the photocurrent density of both samples declines gradually, especially, the photocurrent density of I-ZnO-n disappears more slowly than I-ZnO-m, which suggests that the I-ZnO-n may have the ability of electron storage and release capacity and can produce more reactive oxidative species in the photocatalytic process [44].

The reactive radicals ($\cdot OH$) produced from catalysts under visible light irradiation and in dark have been tested by electron spin resonance (ESR), in which DMPO was used to capture $\cdot OH$. As shown in Fig. 8a, there is no characteristic peak of DMPO·OH in the absence of light. When illuminated by visible light, both the two catalysts show four significant $\cdot OH$ peaks with intensity ratio 1:2:2:1. What's more, the peaks intensity of I-ZnO-n is more than twice as strong as I-ZnO-m, indicating that the $\cdot OH$ concentration produced by I-ZnO-n is much more than that by I-ZnO-m. In generally, $\cdot OH$ are generated from the reactions of electrons or surface oxygen radicals with H_2O in the photocatalyst surface [45]. The surface oxygen radicals mainly result from the migrated e^- and the oxygen vacancies. When we analyzed the correlation between the photocurrent density and free radicals of the two samples, the results showed that the signal strength ratios of I-ZnO-n/I-ZnO-m are 3.2 and 3.4, respectively, which is well consistent with the difference in photocatalytic antibacterial activity between I-ZnO-n and I-ZnO-m.

This results may be ascribed to the smaller grant size and cage structure of I-ZnO-n that are benefit to the separation of photo-excited charge carriers in the photocatalytic antibacterial process. In addition, the surface oxygen vacancy on I-ZnO-n may also promote the separation of photo-excited charge carriers and generate much more free radicals that improve the antibacterial performance [46,47]. In order to further verify that the effect of oxygen vacancy concentration of photocatalytic sterilization, we prepared Iodine-modified ZnO nanomaterials with different oxygen vacancy concentrations by calcining the samples at different calcination times (1 h, 2 h and 3 h) and denoted them as I-ZnO-n-1 h, I-ZnO-n-2 h and I-ZnO-n-3 h, respectively. We tested the oxygen vacancy concentration of the sample. And then, the photocatalytic sterilization activities of the three materials were characterized under visible light irradiation. As can be seen from the figure, with the enhancement of oxygen vacancy signal, the rate of bacterial inactivation increased gradually. The results show that the sample exhibits superior photocatalytic activity with the increasing of oxygen vacancy concentration. (Figure S3)

3.5. Photocatalytic antibacterial mechanism

In order to propose a possible photocatalytic bacterial inactivation mechanism of I-ZnO-n, the light absorption property, band structure and valence band position of the samples were test by DRS、UPS and Mott-Schottky plots, respectively.

Fig. 9 shows the optical absorption properties of two samples that were detected by UV–vis spectrophotometer. Both two samples have certain absorption in the visible region that enables them to be excited by visible light. In addition, the absorption intensity of I-ZnO-n is also stronger than that of I-ZnO-m. This phenomena may be attributed to two factors. The first is that the sample's color affects light absorption. After modified with Iodine, the I-ZnO-n is much darker in color than I-ZnO-m that is good for visible light absorption (insert in Fig. 9a). Another factor may be ascribed to the sample's band narrowing and surface defect states that resulted from Iodine. The samples' energy band structures are estimated from the respective DRS spectra. The I-ZnO-n shows a band gap of c.a. 2.68 eV and I-ZnO-m has a band gap of c.a. 2.92 eV.

Fig. 10 shows the UPS spectra of I-ZnO-n and I-ZnO-m. The illustrations are the part larger version of the full spectra. The secondary-electron onset (E_{onset}) on the right side of the spectrum is 16.43 eV (I-ZnO-n). The work function (WF) of I-ZnO-n was calculated to be 4.79 eV, which is determined from the secondary-electron onset as WF = $h\nu$- E_{onset} ($h\nu$ = 21.22 eV). The corresponding Fermi energy level
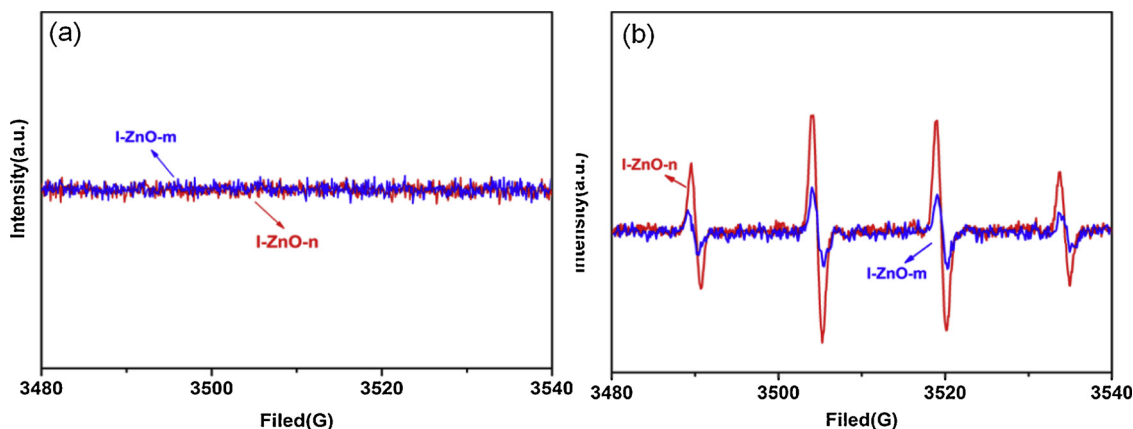
Fig. 8. DMPO spin-trapping ESR spectra recorded at ambient temperature in dark (a) and under visible light irradiation (b).

(E_F) is -4.79 eV. The Valence Band maximum (E_{VB}) was calculated to be -6.98 eV for I-ZnO-n (versus vacuum). According to the relationship between the vacuum energy (E_{abs}) and the normal hydrogen electrode potential (E^θ) [48]: E_{abs} = -E^θ- 4.44, the corresponding valence (VB) are 2.54 eV for I-ZnO-n (versus SHE). According to the same calculation method, the WF, E_F, E_{VB} and VB of I-ZnO-m were found to be 4.77 eV, -4.77 eV, -6.84 eV and 2.4 eV, respectively. Considering the band gap energy (E_g) value (2.68 eV for I-ZnO-n and 2.92 eV for I-ZnO-m) that were obtained from the UV–vis diffusion reflectance spectra, the location of minimum of the Conduction Band (CB) can be calculated as -0.14 eV for I-ZnO-n and -0.52 eV for I-ZnO-m. This result was further confirmed by Mott-Schottky plots as shown in Fig. 11.

According to the linear method, the Conduction Band (CB) of I-ZnO-m and I-ZnO-n can be determined to be -0.54 eV and -0.15 eV, respectively. The result is consistent with the consequence from UPS and DRS.

Based on the above characterization, a possible photocatalytic bacterial inactivation mechanism of I-ZnO-n was proposed and showed in Scheme 1. The smaller size of ZnO and modification of Iodine enhance the number of oxygen vacancies on ZnO surface. The oxygen vacancies break the electrical neutrality of ZnO. To balance neutral, the Zn^{2+} around oxygen vacancy transform into Zn^+ and the other e^- was bound by the oxygen vacancy. The more numbers of the oxygen vacancy in ZnO has, the more binding electrons exist around oxygen vacancies. All the binding electrons form donor impurity level under the CB minimum of the sample. Under visible light irradiation, the binding electrons are easily activated from donor levels to the CB of ZnO. The electrons on ZnO surface are captured by O_2 to form ROS. In addition, both in dark and under visible light irradiation, the oxygen defects in I-ZnO-n can be easily ionized oxygen vacancies (V_O^+) and react with the water or O_2 to product reactive oxygen species (ROS) such as·OH. These
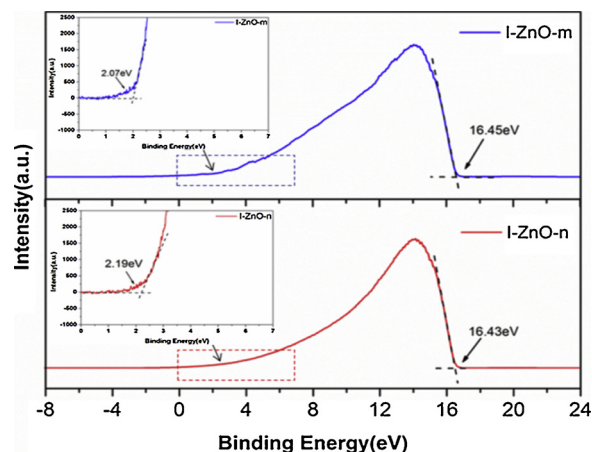

Fig. 10. UPS spectra of I-ZnO-m (a) (c) and I-ZnO-n (b) (d).

ROS inactivate the bacteria by attacking the bacterial cell.

4. Conclusions

In general, Iodine-modified ZnO with cage structure (I-ZnO-n) were prepared by reflux method successfully. I-ZnO-n shows strong absorption in visible light and exhibits better photocatalytic antibacterial activity towards *E.coli* than that of ZnO and I-ZnO-m. The modification of Iodine and cage structure makes it has more surface oxygen vacancy defects, which is benefit for the separation of photogenerated electron hole pairs and significantly improve its photocatalytic performance.
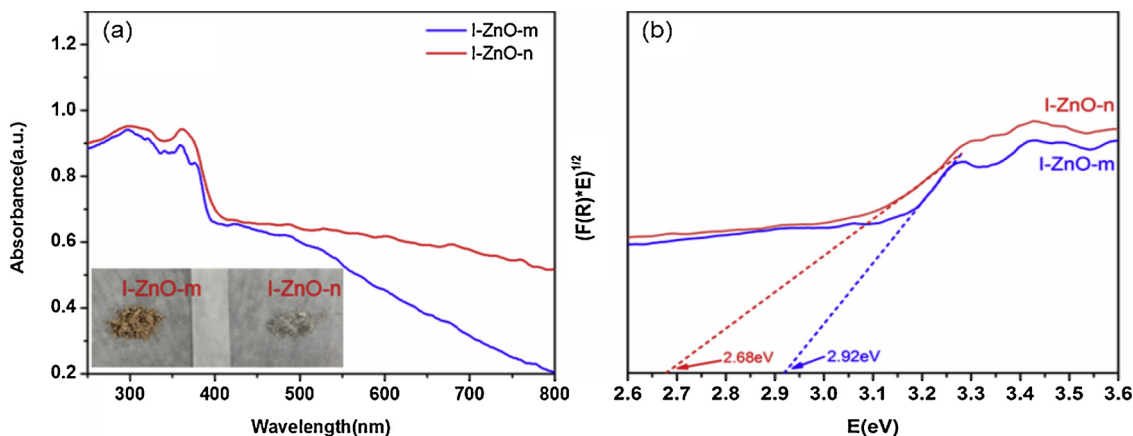

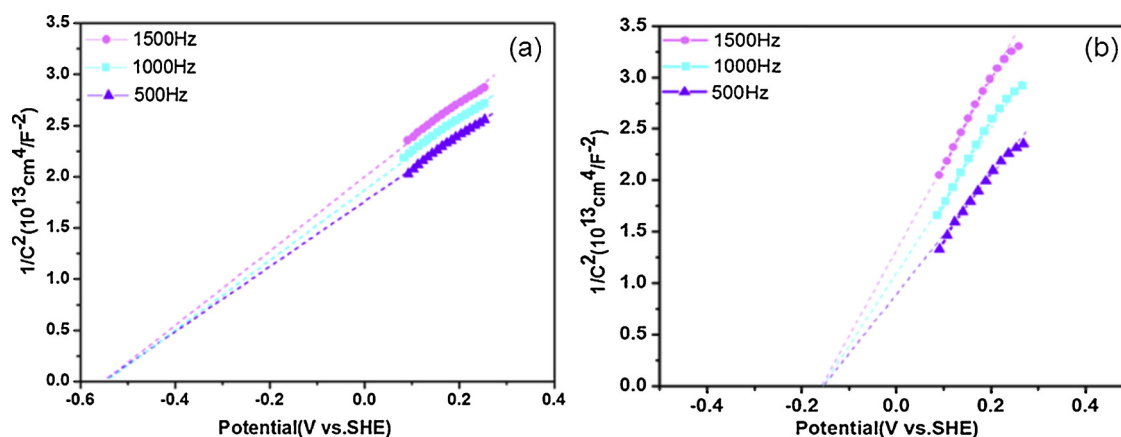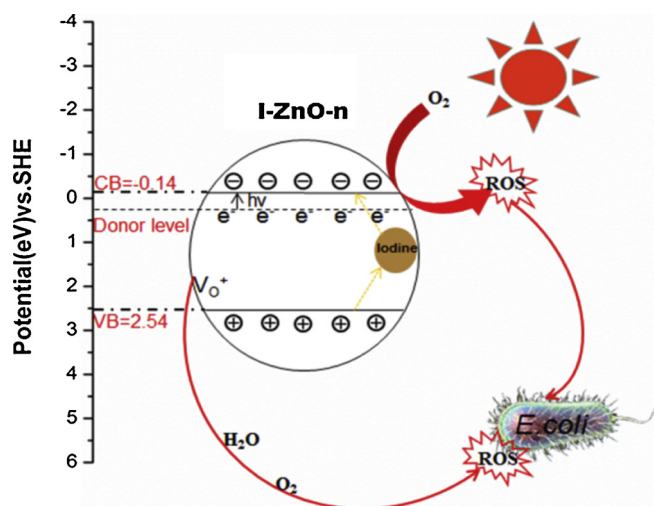**Fig. 9.** UV-vis diffusion reflectance spectra of I-ZnO-m and I-ZnO-n.

Fig. 11. Mott-Schottky plots of I-ZnO-m (a) and I-ZnO-n (b).

Scheme 1. Possible mechanism of photocatalytic bacterial inactivation under visible light using I-ZnO-n.

Conflict of interest

Nothing declared.

Acknowledgements

Appendix A. Supplementary data

Supplementary material related to this article can be found, in the online version, at doi:https://doi.org/10.1016/j.apcatb.2019.117873.

References

[1] Y. Guan, B.J. Zheng, Y.Q. He, X.L. Liu, Z.X. Zhuang, C.L. Cheung, S.W. Luo, P.H. Li, L.J. Zhang, Y.J. Guan, K.M. Butt, K.L. Wong, K.W. Chan, W. Lim, K.F. Shortridge, K.Y. Yuen, J.S.M. Peiris, L.L.M. Poon, Science 302 (2003) 276.
[2] W.B. Park, N.-J. Kwon, P.G. Choe, S.-J. Choi, H.S. Oh, S.M. Lee, H. Chong, J.-I. Kim, K.-H. Song, J.H. Bang, E.S. Kim, H.-B. Kim, S.W. Park, N.J. Kim, M.-d. Oh, J. Korean Med. Sci. 31 (2016) 315–320.
[3] M.-K. Lee, S. Kim, M.-N. Kim, O.J. Kweon, Y.K. Lim, C.-S. Ki, J.-S. Kim, M.-W. Seong, H. Sung, D. Yong, H. Lee, J.-R. Choi, J.-H. Kim, Ann. Lab. Med. 36 (2016) 154–161.
[4] C. Wang, J. Luo, J. Wang, W. Su, S. Gao, M. Zhang, L. Xie, H. Ding, S. Liu, X. Liu, Y. Chen, Y. Jia, H. He, Integr. Zool. 9 (2014) 372–375.
[5] X. Ni, F. He, M. Hu, X. Zhou, B. Wang, C. Feng, Y. Wu, Y. Li, J. Tu, H. Li, M. Liu,
H. Chen, S. Chen, Microbes Infect. 17 (2015) 48–53.
[6] S. Wu, S. Xu, X. Chen, H. Sun, M. Hu, Z. Bai, G. Zhuang, X. Zhuang, Sci. Rep.-UK 8 (2018) 8220.
[7] R. Smart, D.F. Spooner, J. Soc. Cosmet. Chem. 23 (1972) 721–737.
[8] F. Cappitelli, C. Sorlini, Appl. Environ. Microb. 74 (2008) 564.
[9] Y. Lan, C. Hu, X. Hu, J. Qu, Appl. Catal. B: Environ. 73 (2007) 354–360.
[10] G. Joanne, Z. Zhang, Int. J. Photoenergy (2010).
[11] X. Wang, T.-T. Lim, Water Res. 47 (2013) 4148–4158.
[12] T. Matsunaga, R. Tomoda, T. Nakajima, H. Wake, FEMS Microbiol. Lett. 29 (1985) 211–214.
[13] V. Etacheri, G. Michlits, M.K. Seery, S.J. Hinder, S.C. Pillai, ACS Appl. Mater. Interfaces 5 (2013) 1663–1672.
[14] H. Lin, W. Deng, T. Zhou, S. Ning, J. Long, X. Wang, Appl. Catal. B: Environ. 176-177 (2015) 36–43.
[15] W. Deng, S. Ning, Q. Lin, H. Zhang, T. Zhou, H. Lin, J. Long, Q. Lin, X. Wang, Colloids Surf. B 144 (2016) 196–202.
[16] S. Ning, H. Lin, Y. Tong, X. Zhang, Q. Lin, Y. Zhang, J. Long, X. Wang, Appl. Catal. B: Environ. 204 (2017) 1–10.
[17] S. Bykkam, S. Narsingam, M. Ahmadipour, T. Dayakar, K. Venkateswara Rao, C. Shilpa Chakra, S. Kalakotla, Superlattice. Microst. 83 (2015) 776–784.
[18] V. Lakshmi Prasanna, R. Vijayaraghavan, Langmuir 31 (2015) 9155–9162.
[19] J. Podporska-Carroll, A. Myles, B. Quilty, D.E. McCormack, R. Fagan, S.J. Hinder, D.D. Dionysiou, S.C. Pillai, J. Hazard. Mater. 324 (2017) 39–47.
[20] D.H. Piva, R.H. Piva, M.C. Rocha, J.A. Dias, O.R.K. Montedo, I. Malavazi, M.R. Morelli, Adv. Powder Technol. 28 (2017) 463–472.
[21] K. Kairyte, A. Kadys, Z. Luksiene, J. Photochem. Photobiol. B 128 (2013) 78–84.
[22] D. Guo, C. Wu, H. Jiang, Q. Li, X. Wang, B. Chen, J. Photochem. Photobiol. B 93 (2008) 119–126.
[23] R. Kumar, S. Anandan, K. Hembram, T. Narasinga Rao, ACS Appl. Mater. Interfaces 6 (2014) 13138–13148.
[24] J. Wróbel, J. Piechota, Phys. Status. Solidi. B 244 (2007) 1538–1543.
[25] X. Liu, Q. Hu, Q. Wu, W. Zhang, Z. Fang, Q. Xie, Colloids Surf. B 74 (2009) 154–158.
[26] A. Wolcott, W.A. Smith, T.R. Kuykendall, Y. Zhao, J.Z. Zhang, Adv. Funct. Mater. 19 (2009) 1849–1856.
[27] S. Chakrabarti, B.K. Dutta, J. Hazard. Mater. 112 (2004) 269–278.
[28] P. Banerjee, S. Chakrabarti, S. Maitra, B.K. Dutta, Ultrason. Sonochem. 19 (2012) 85–93.
[29] A. Sapkota, A.J. Anceno, S. Baruah, O.V. Shipin, J. Dutta, Nanotechnology 22 (2011) 215703.
[30] J. Wang, F. Qu, X. wu, Sci. Adv. Mater. (5) (2013) 1052–1059.
[31] P. Nagarajan, V. Rajagopalan, Sci. Technol. Adv. Mater. 9 (2008) 035004-035004.
[32] Z. Zhang, C.-C. Wang, R. Zakaria, J.Y. Ying, J. Phys. Chem. B 102 (1998) 10871–10878.
[33] Q.-Y. Lin, Q. Lin, Y.-Q. Zhang, H.-X. Lin, T.-H. Zhou, S.-B. Ning, X.-X. Wang, Res. Chem. Intermedia. 43 (2017) 5067–5081.
[34] G. Murillo, E. Leon-Salguero, P.R. Martínez-Alanis, J. Esteve, J. Alvarado-Rivera, F. Güell, Nano Energy 60 (2019) 817–826.
[35] Za. Huang, Z. Wang, K. Lv, Y. Zheng, K. Deng, ACS Appl. Mater. Interfaces 5 (2013) 8663–8669.
[36] R. Yang, J. Cai, K. Lv, X. Wu, W. Wang, Z. Xu, M. Li, Q. Li, W. Xu, Appl. Catal. B: Environ. 210 (2017) 184–193.
[37] M. Schumm, M. Koerdel, J.F. Morhange, Z. Golacki, K. Grasza, P. Skupinski, W. Szuszkiewicz, H. Zhou, V. Malik, H. Kalt, C. Klingshirn, J. Geurts, J. Phys. Conf. Ser. 92 (2007) 012149.
[38] L.-h. Xiao, K.-p. Sun, X.-l. Xu, X.-n. Li, Catal. Commun. 6 (2005) 796–801.
[39] S. Moulay, J. Polym. Eng. 33 (2013) 389–443.
[40] P. Šimek, K. Klímová, D. Sedmidubský, O. Jankovský, M. Pumera, Z. Sofer, Nanoscale 7 (2015) 261–270.
[41] M. Gao, J. Yang, T. Sun, Z. Zhang, D. Zhang, H. Huang, H. Lin, Y. Fang, X. Wang, Appl. Catal. B: Environ. 243 (2018) 734–740.
[42] Y. Zhang, C. Lin, Q. Lin, Y. Jin, Y. Wang, Z. Zhang, H. Lin, J. Long, X. Wang, Appl. Catal. B: Environ. 235 (2018) 238–245.

[43] Q. Liu, F. Wang, H. Lin, Y. Xie, N. Tong, J. Lin, X. Zhang, Z. Zhang, X. Wang, Surface oxygen vacancy and defect engineering of WO3 for improved visible light photo-catalytic performance, Catal. Sci. Technol. 8 (2018) 4399–4406.

[44] W. Wang, J. Yu, Q. Xiang, B. Cheng, Appl. Catal. B: Environ. 119–120 (2012) 109–116.

[45] Q. Xiao, Z. Si, J. Zhang, C. Xiao, X. Tan, J. Hazard. Mater. 150 (2008) 62–67.

[46] H. Tan, Z. Zhao, W.-b. Zhu, E.N. Coker, B. Li, M. Zheng, W. Yu, H. Fan, Z. Sun, ACS. Appl. Mater. Interfaces 6 (2014) 19184–19190.

[47] L. Ye, K. Deng, F. Xu, L. Tian, T. Peng, L. Zan, Phys. Chem. Chem. Phys. 14 (2012) 82–85.

[48] G. Xiao, X. Wang, D. Li, X. Fu, J. Photochem. Photobiol. A 193 (2008) 213–221.